Acta Crystallographica Section A
Foundations of Crystallography
ISSN 0108-7673

Received 16 September 2002
Accepted 6 January 2003

Experimental lensless soft-X-ray imaging using iterative algorithms: phasing diffuse scattering

H. He,[a] S. Marchesini,[a] M. Howells,[a] U. Weierstall,[b] G. Hembree[b] and J. C. H. Spence[b]*

[a]Advanced Light Source, Lawrence Berkeley Laboratory, 1 Cyclotron Road, Berkeley, CA 94720, USA, and [b]Department of Physics, Arizona State University, Tempe, AZ 85287, USA. Correspondence e-mail: spence@asu.edu

Images of randomly placed two-dimensional arrays of gold balls have been reconstructed from their soft-X-ray transmission diffraction patterns. An iterative hybrid input–output (*HiO*) algorithm was used to solve the phase problem for the continuous distribution of diffuse X-ray scattering. Knowledge of the approximate size of the clusters was required. The images compare well with scanning electron microscope (SEM) images of the same sample. The use of micrometre-sized silicon nitride window supports is suggested, and absorption filters have been used to allow collection of low spatial frequencies often obscured by a beam stop. This method of phasing diffuse scattering may have application to scattering from individual inorganic nanostructures or single macromolecules.

1. Introduction

This paper describes the reconstruction of images of two-dimensional non-periodic objects from their experimental coherent soft-X-ray transmission speckle diffraction patterns. It follows previous experimental work on the inversion of coherent optical (Cederquist *et al.*, 1988; Kamura & Komatsu, 1998), X-ray (Miao *et al.*, 1999; Robinson *et al.*, 2001) and electron (Weierstall *et al.*, 2001) diffraction data, based on theoretical work by Sayre *et al.* (Sayre, 1952, 1980; Sayre *et al.*, 1998), Gerchberg & Saxton (1972), Fienup (1982) and others. The object consists of an array of randomly positioned gold balls of 50 nm diameter, illuminated by the coherent soft-X-ray beam generated by an undulator at the Advanced Light Source (ALS) storage ring at Lawrence Berkeley Laboratory. SEM images of the same object are used to evaluate the veracity of the iterative hybrid input–output (*HiO*) algorithm (Fienup, 1982), which was used to reconstruct the images. We briefly describe the prospects for further development of this lensless imaging technique. The work is aimed at image reconstruction without the need for additional low-resolution images obtained with a lens, as used in previous work, to provide the low spatial frequencies obscured by a beam stop. We describe the use of absorption filters to address this problem, but find that, for our clustered objects, low-resolution images are still needed to provide a sufficiently accurate support. Supports based on the autocorrelation function are also explored.

A considerable literature describes various approaches to the phase problem for non-periodic objects [for a review, see Stark (1987)]. These include developments of the powerful Gerchberg–Saxton–Fienup hybrid input–output (*HiO*) algorithm (Gerchberg & Saxton, 1972; Fienup, 1982), approaches based on analyticity and complex zeros (Liao *et al.*, 1997), the study of projections onto convex sets [see Bauschke *et al.* (2002) for recent work] and use of the transport of intensity equations (Paganin & Nugent, 1998). A summary of work on all these methods can be found in the workshop summary given in Spence *et al.* (2001). These methods have been used to phase experimental far- and near-field radiation fields in areas as diverse as neutron scattering, laser scattering and coherent electron nanodiffraction (Weierstall *et al.*, 2001). Despite the success of simulations that include noise, however, experimental results remain scarce. A notable exception is the striking tomographic images which have been reconstructed from coherent soft and hard X-ray scattering from non-periodic objects using the *HiO* algorithm and its developments, in combination with low-resolution imaging by other methods, by Miao and colleagues (Miao *et al.*, 1999, 2002), based on the approach of Sayre (1980), who refer to the method as oversampling. The method is akin to the solvent-flattening, fragment-completion and density-modification methods of crystallography, which have been analyzed in detail using the concept of a confined structure (De Caro *et al.*, 2002). The emphasis on oversampling makes connection with the use of non-crystallographic symmetries to assist in solving the phase problem for crystals [see Millane (1990) for a review]. The *HiO* algorithm iterates between real and reciprocal space, applying known constraints in each domain. The most important three of these are the known sign of the charge density in real space, its measured Fourier modulus, and a known support (the region in real space within which the object is non-zero). Outside the support, the X-ray beam passes unobstructed, hence this portion of the object is

'known', just as the density of the water jacket around a crystallized protein is known, and this known information compensates for the loss of phase information. In using the algorithm, a set of randomly chosen phases are used for the diffraction pattern initially, and the final result must be independent of this choice. For small phase shifts in two dimensions, the signs of both the real and imaginary parts of the object wavefunction are also known (Miao *et al.*, 1999). Sampling in the diffraction pattern of a non-periodic object is finer than the Nyquist rate for the charge density (at which Bragg beams would appear if the charge density were periodically continued) and corresponds to that required for Nyquist sampling of the autocorrelation function of the isolated object (Sayre, 1952). By thus coherently diffracting from an area at least, say, four times as large as the object, for which most of this total area (outside the support) consists of 'known' material with unit transmission, it is not surprising that the phase problem can be solved. An error metric is defined which measures agreement between the known (unity) value of the object transmission function outside the support of the isolated object and the current estimate – a small result indicating that the three constraints have been satisfied. The result for zero error has been shown to be unique (and thus correct inside the support) in all but pathologically rare cases (Barakat & Newsam, 1984) for two-dimensional complex objects. This error is a useful guide to convergence only for the error-reduction algorithm. For complex objects with large phase shifts, the signs of the complex image are unknown. However, it has been shown that by the use of a disjoint support consisting of sufficiently separated regions (such as some of our clusters), complex objects may be reconstructed (Fienup, 1987). A sufficient separation satisfies the conditions for Fourier transform holography (Howells *et al.*, 1999). However, in this case the accuracy with which the support needs to be known increases greatly. For three-dimensional objects, reciprocal space may be filled with data before iterating using three-dimensional Fourier transforms, and a known volume which encloses the object may be used as a support (Miao *et al.*, 2001). Then it is found that the convergence properties of *HiO* are improved, since the three-dimensional problem is overdetermined by a factor of two (Millane, 1993). Only the phase change per voxel need be small in order to apply a sign constraint, rather than the total phase charge along an optical path parallel to the beam through a two-dimensional object.

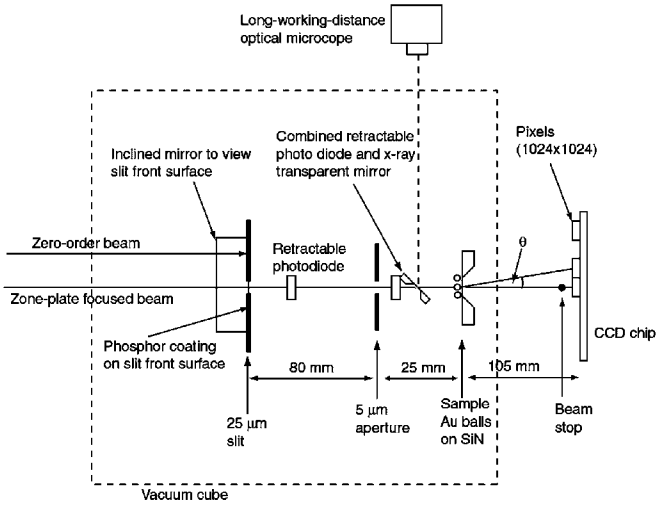

Figure 1
Side view of chamber. The inclined mirror allows viewing of the energy spectrum from the side of the chamber on phosphor. X-ray transparent mirrors were made using silicon nitride windows to reflect visible light, avoiding the need for a hole. An absorption filter (6 μm, aluminium) before the inclined mirror was used to record the inner region of the pattern around the beam stop. Photodiodes and phosphor screens are used to align apertures and the zone plate. The beam stop is a 1 mm diameter brass bead on a 0.1 mm wire across the CCD. Sample and aperture stages not shown.

Experimentally, implementation of the *HiO* algorithm is difficult. Samples usually consist of an isolated object supported on an X-ray-transparent silicon nitride window. Given typical 1024×1024 pixel CCD (charge-coupled device) detectors, the size of the object is severely limited. For example, with oversampling by two in each dimension and a final resolution of 10 nm per pixel in the reconstruction, the overall width of the empty area plus object must be known *a priori* to be less than 5 μm. The handling, placement and goniometer design for such isolated objects is difficult. Dilute suspensions of organic structures in amorphous ice (as used in cryomicroscopy) may provide a solution, if the increase in radiation damage with resolution does not prove prohibitive (Spence, 2003).

In addition to the problem of knowing *a priori* the boundary of the isolated object, a second serious practical difficulty with the *HiO* approach results from the need for a beam stop of significant size in the transmission geometry, which results in the loss of low-spatial-frequency information. This problem has been addressed in the past by using the *HiO* oversampling method in combination with an independent low-resolution image of the object (*e.g.* from SEM, X-ray zone plate or optical image) to provide the low spatial frequencies. A further difficulty with the *HiO* method is the practical problem of finding the isolated sample (which is too small to be seen with our external optical microscope) with the X-ray beam. Here the X-ray shadow image of the sample as formed by edge scattering at the illumination aperture is of some use. In this paper, we address the beam-stop problem by using absorption filters to reduce intensity and so minimize the loss of low-angle scattering. We address the problem of making an isolated object through the use of very small silicon nitride membranes. We also demonstrate the value of the autocorrelation function to provide a direct image in the case where the object contains some isolated point scatterers, such as gold balls. Using both this 'heavy-atom' method and the *HiO* algorithm, we obtain reconstructed images of 50 nm diameter balls with about seven pixels along the ball diameter.

2. Experimental

Fig. 1 shows the experimental arrangement. All items except the monochromator are fitted to a 6 in MDC UHV cube.

Mechanical (lateral tilt/vertical translate) coarse X, Y motions support from below through miniflanges the energy-dispersion slit and the field-limiting aperture, for which fine X, Y motion is provided by a piezo stage. The sample stage consists of crossed miniature Newport UMR3.5V6 stages driven by New Focus 830X-V picomotors. The detector is a Princeton nude soft X-ray PI-SX:1024/TE CCD camera with 24 μm pixels, mounted on an opening portal door with *O*-ring seal for simple sample exchange. The working distance from sample to camera was 105 mm. Two beam-stop bars spanning wide forks on linear motion feedthroughs were installed in orthogonal directions across the detector. These could be inserted separately during successive recordings, and the patterns added together, to produce a square of missing data in the center. A later improved arrangement, which avoids the need for merging data, consisted of a 1 mm diameter bead on a 0.1 mm wire spanning the same fork. By taking advantage of slight bending of the wire and the Friedel symmetry of the patterns, it was possible to record all the data except that obstructed by the bead. By withdrawing the fork, the intensity behind the beamstop could be recorded after insertion of a 6 μm thick aluminium foil absorption filter. An external optical microscope is used to find the beam, using a small dot of phosphor near the sample and an eyepiece graticule. (After centering the beam on the phosphor at the graticule center, the sample is brought to the stationary graticule cross hairs with the stage motions). Silicon nitride windows coated with aluminium were found to make excellent 45° optical mirrors which allowed the source side of the sample to be viewed with the beam on. A novel zone-plate monochromator was used, described in detail elsewhere (Howells *et al.*, 2003). This gives a fractional monochromaticity at 600 eV of 0.2% and is used in first order. The outermost zone width is 0.34 μm, and the structure consists of a 0.75 mm square off-axis portion of a nominal 5.31 mm diameter plate (of 3901 zones). The focal length is 874 mm. The zone plate is etched into a silicon nitride window, coated with aluminium on both sides to provide mechanical support and heat removal. By manually scanning the dispersion slit (which lies at the approximate focus of the zone plate) vertically, a spectrum could be read out from the photodiode one, and the intense first-order line isolated. A screen for observing this spectrum was mounted beside the slits, which could be observed through a mirror.

Considerable difficulties were encountered with stray light and stray X-rays, which must be minimized in view of the very small X-ray scattering volume. The region between sample and CCD camera was filled with a removable cone to minimize stray light generated, for example, from the phosphors in the chamber. Every metal foil aperture acts as a point source of X-rays at its edges, and these point sources produce shadow images at the detector of every subsequent X-ray transparent object. (The suggestion has been made that the rim of a second aperture should lie around the first minimum of the diffraction pattern from a first aperture, thereby minimizing stray edge scattering.) The effects of diffraction broadening in the beam as it propagates beyond apertures can be significant at these wavelengths and propagation distances. The distances indicated in Fig. 1 were chosen to minimize these artifacts, with the zone-plate monochromator focused on the 5 μm illumination aperture. When silicon nitride windows larger than about 50 μm were used to support the sample, the shadow image on the CCD of the window projected from a point source on the edge of the field-limiting aperture could be arranged to be smaller than the beam stop. For the very small windows used (a few μm), the far-field diffraction pattern of the window itself produces a sinc-function-like distribution at the center of the pattern. Diffraction broadening of the direct beam from the 5 μm field-limiting aperture at the detector produces a total beam width smaller than one CCD pixel. Nevertheless, severe 'blooming' effects were observed extending about 1 mm from the center, resulting in the loss of low-spatial-frequency information. (This may actually be due to stray scattering from roughness in the 5 μm aperture on a scale larger than the wavelength.) For this reason, in previous work it has been necessary to use an image obtained by a different technique (*e.g.* X-ray zone-plate microscope) to supply these missing low spatial frequencies. In this paper, we have attempted to address this 'beam-stop' problem by other means, including the use of an absorption filter and a wide range of recording times.

Samples were made by placing a droplet of solution containing 'gold conjugate' colloidal gold balls on a silicon nitride window (thickness 100 nm) and allowing it to dry. The samples were also imaged by a field-emission scanning electron microscope (SEM).

The choice of experimental parameters is governed by the following considerations. We define the object support as the boundary of an object of width D. The essential requirement for the success of the *HiO* algorithm is the use of an isolated object of size D with compact support, where D is known approximately, within a larger field of width $W > 2D$, from which the diffraction pattern is obtained. The density in the region outside the support must be known – in our case this is the transmissivity of the silicon nitride supporting membrane, assumed to be unity. If $W > 2D$, solution of the phase problem is possible, since most of the object is then known, having transmissivity unity. It follows that coherent diffraction is required from a region of width $W > 2D$, a condition said to provide 'oversampling'. (In fact, this condition provides correct Nyquist sampling of the entire object and diffraction pattern, if we consider the known bordering region outside the object support as part of the 'object'.). If the first-order CCD pixel (adjacent to the central pixel) subtends angle θ as shown in Fig. 1, then the camera length L must be chosen such that $W = \lambda/\theta$ to provide adequate 'oversampling'. With our 24 μm pixels and $L = 105$ mm, taking $\lambda = 2.11$ nm at 588 eV, we have $W = 9.23$ μm, which must be less than the lateral coherence width of the beam. Temporal coherence must also not limit interference between points at this spacing.

The formation of an *isolated* test object much smaller than 9 μm, while ensuring that no other material contributes to the diffraction pattern, proved difficult. In preliminary work, we found that the use of very small silicon nitride windows (a few μm across) has many advantages, since a drop of dilute solu-

tion containing the objects of interest may be placed on the window to dry. The object is then isolated by the transparent portion of the window. In addition, these windows: (i) reduce stray light into the detector area; (ii) greatly reduce 'blooming' at the center of the detector, by reducing the overall X-ray signal from areas other than the sample; (iii) the crystallographic wedge facets around the window make a soft aperture, which eliminates stray X-ray scattering from edge roughness on laser-drilled metal foil apertures; the wedge angle, between (100) and (111) facets of silicon, is 54° (attempts to apply the *HiO* algorithm to objects filling small holes in opaque screens were unsuccessful owing to this edge scattering); (iv) the windows produce a diffraction pattern in the beam-stop region that is useful for orientating and scaling the data to the support.

It is not possible, however, to use the physical boundary of the window as a support function to be applied in the iterations. The 54° wedge shape of the window boundaries is partially transparent, so that a border region of a μm or so exists, on which gold balls will contribute to the diffraction pattern. (At 600 eV, the linear attenuation distance in silicon is 0.6 μm.) As discussed in previous work, for real two-dimensional objects, a computational triangle of arbitrary shape enclosing the object may be used as a support. Our objects behave as real if the phase shift Θ [see equation (1) below] introduced by scattering is less than $\pi/2$, in which case a sign constraint may be applied, in which the signs of both the real and imaginary parts of the image are set positive. When the border of partially transparent material is included, the oversampling condition may not be fulfilled for such a support shape, and the additional phase shift introduced by the silicon may exceed $\pi/2$. (For gold, the phase shift is 0.36 rad per 30 nm thickness at 588 eV.) We have therefore used small loops drawn around the isolated clusters as a disjoint support, setting the amplitude in the image to zero outside these loops in each iteration of *HiO*. The loop shapes can be obtained either from the autocorrelation function (the transform of the diffracted intensity), which overestimates the number of loops, or from the SEM image. The *HiO* algorithm is then expected to provide the image detail inside these loops.

3. Results

Fig. 2(*a*) shows the experimental diffraction pattern obtained from a set of 50 nm diameter gold ball clusters lying on a silicon nitride window about 2.5 μm square. The beam energy was 588 eV and the working distance 105 mm. The pattern shows fine speckle fringes (owing to interference between different balls) that modulate the Airey disc-like pattern expected from a single ball. A recognizable pattern is obtained after about 10 s. Fig. 2(*a*) shows data accumulated over several hours. Small deviations from inversion symmetry in the pattern were observed – for a real object the pattern must be symmetric. The pattern shown has been made symmetrical by inversion averaging. Some of the central region exceeds the dynamic range of the CCD but is recorded separately with an absorption filter inserted to allow safe removal of the beam stop from the X-ray path. For later comparison purposes, Fig. 2(*b*) shows the Fourier transform of the intensity of the SEM image of the sample, which is not expected to be identical to

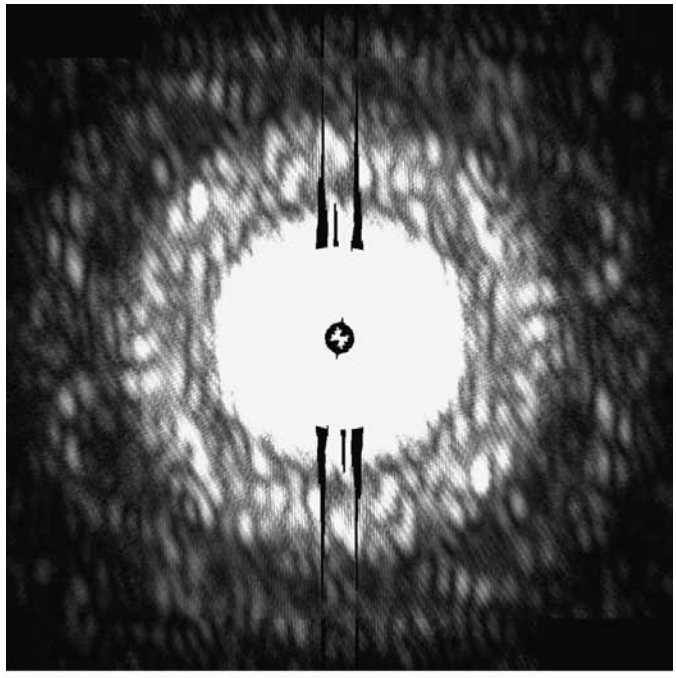

(*a*)

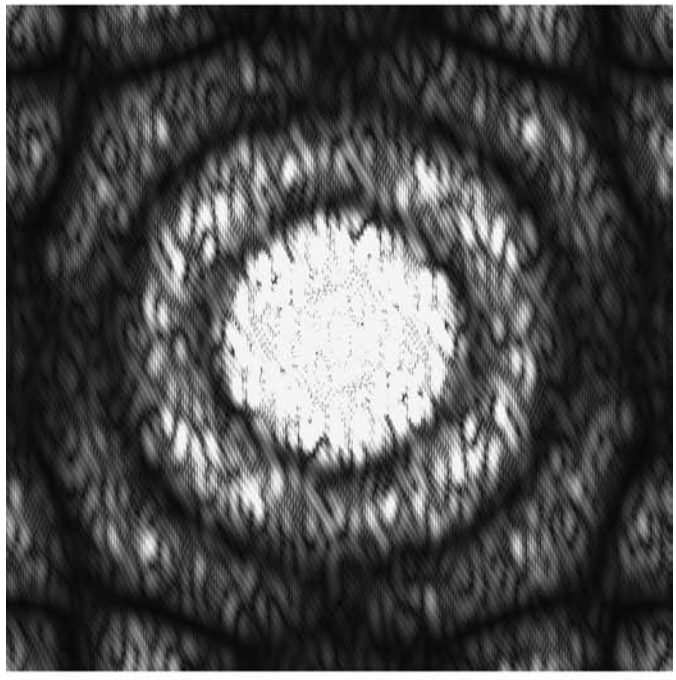

(*b*)

Figure 2
(*a*) Experimental soft X-ray transmission diffraction pattern (Au5010) from clusters of 50 nm diameter gold balls lying on a transparent membrane. X-ray wavelength 2.11 nm (588 eV), working distance 105 mm. The central region exceeds the dynamic range of display. The pattern has been averaged by inversion and contains artifacts from camera readout. (*b*) Simulated diffraction pattern based on ball positions obtained from a SEM image of the same object. SEM image and extracted ball positions are shown in Figs. 5(*a*) and (*b*), respectively.

the X-ray pattern from our phase objects. Fig. 3(*a*) shows the innermost region and the beam stop, revealing the subsidiary minima in the diffraction pattern from the window itself. Fig. 3(*b*) shows a simulation of this pattern, discussed below. The orientation of these minima was useful for determining the orientation of the support mask imposed on the object reconstruction.

Simulations were performed for the diffraction pattern from a phase sphere with transmission function

$$T(\mathbf{r}) = \exp[2\pi i n t(\mathbf{r})/\lambda] = a\exp(i\theta) = a\cos\theta + ia\sin\theta, \quad (1)$$

where $\mathbf{r}$ is a two-dimensional vector, $t(\mathbf{r})$ is the projected thickness of the sphere, and $n = (1 - \delta) - i\beta = 1 - 0.004\,091\,76 - i0.003\,528\,67$ is the refractive index of gold at 588 eV. This introduces a phase shift of about 0.6 rad for a thickness of 50 nm of gold at 588 eV, within the limit of the small-angle approximation needed for use of the sign constraint in the

(*a*)

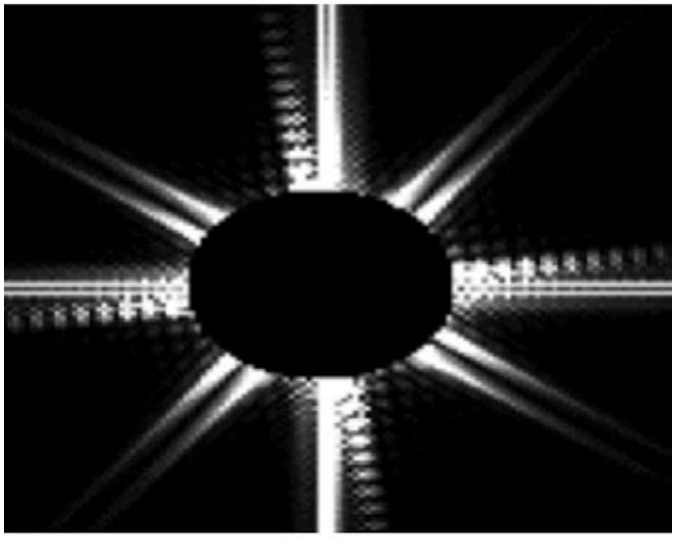

(*b*)

Figure 3
(*a*) Central region of a pattern similar to Fig. 2, showing 1 mm beam-stop bead and the sinc-function-like pattern from the silicon nitride window. In addition to the subsidiary minima from the window, additional streaks are seen which arise from the valleys running from the corners of the SiN windows. (*b*) Simulated soft-X-ray diffraction pattern from silicon nitride window with 54° wedge-shaped borders. The pattern is in good agreement with (*a*).

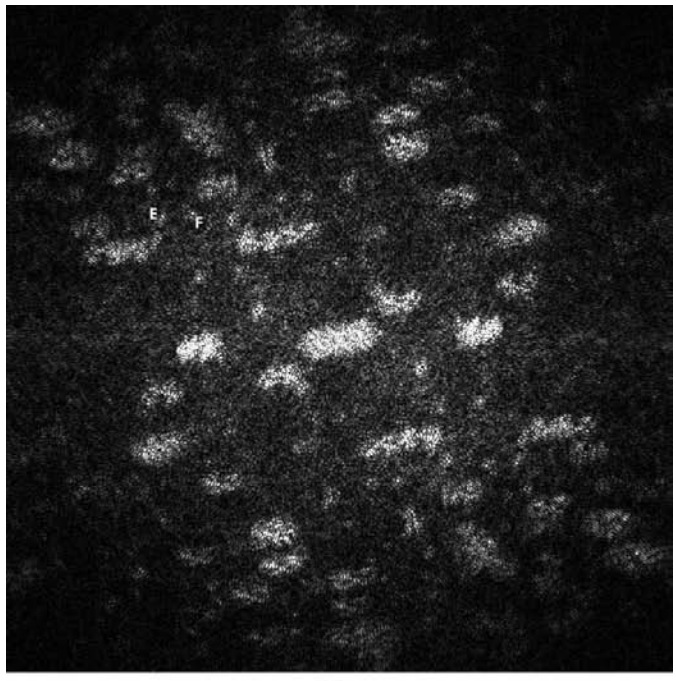

(*a*)

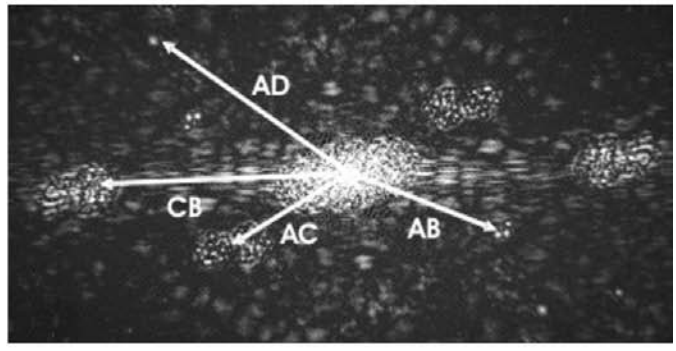

(*b*)

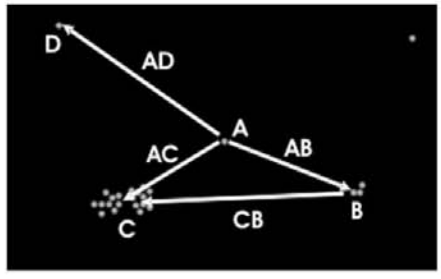

(*c*)

Figure 4
(*a*) Fourier transform of the intensity distribution shown in Fig. 2(*a*). This is the autocorrelation (Patterson) function of the object. Note single ball features at *E* and *F*, which correspond to the balls in the SEM image Fig. 5(*a*) marked *E* and *F*. (*b*) Enlarged portion of autocorrelation function, showing real-space images of several clusters as formed by convolution with the autocorrelation of one isolated ball. In (*c*) is shown the real-space structure obtained from the SEM image, indicating the inter-ball vectors identified in (*b*).

reconstruction, which assumes that ($a \cos\theta$) and ($a \sin\theta$) are positive. In general, the modulus $I(\mathbf{u})$ of the Fourier transform of $T(\mathbf{r})$ does not have inversion symmetry. For small θ, however, it does, and this ''Friedel's law'' behavior may be used as a test for the more readily inverted 'real object'. For our special case of a random collection of symmetric objects, $I(\mathbf{u})$ also has inversion symmetry for all θ. Simulations show that the first minimum of the pattern from a single phase ball occurs at a value of $\sin\theta/\lambda = 1.394/d$ ($d = 50$ nm, $\lambda = 2.11$ nm), where d is the diameter of the ball and θ is the semiangle subtended at the sample by the first minimum in the diffraction pattern (Fig. 1). (The factor 1.394, which depends on the refractive index of the ball, is replaced by 1.22 for the Airey disc pattern from an opaque ball.) This result can also be used to scale the data. The *HiO* algorithm was always successful in rapidly recovering the correct image from simulated diffraction intensity data, using a triangular support shape which included all balls, even in the presence of simulated Poisson noise.

Fig. 4(*a*) shows the experimental autocorrelation function of the object obtained by Fourier transform of Fig. 2. This is a map of all inter-ball vectors transferred to common origin. In Fig. 4(*b*), we show an enlarged portion of this map, with a sketch of the real-space structure below in Fig. 4(*c*) obtained from a SEM image. Because the structure contains at least one isolated ball (*e.g.* A in Fig. 4*c*), the autocorrelation function includes an image of every cluster convoluted with the single ball A, and these images form a faithful representation of the structure in real space. (This is analogous to the heavy-atom method of crystallography.) Thus, Fig. 4(*b*) already provides useful images of several clusters (*e.g.* cluster B) without iterative processing. These images can also be used to generate a support function.

Fig. 5(*a*) shows a SEM image of the same sample used to obtain the diffraction pattern in Fig. 2 (data set Au5010), including the area around the X-ray-transparent window, which is seen to be about 2 μm on a side. Fig. 5(*b*) shows a map of ball positions extracted from the SEM image. The positions of one isolated ball (A) and a cluster of three balls (B) are noted in the image. The corresponding peaks these balls generate in the autocorrelation function are indicated in Fig. 4(*b*). Fig. 6 compares the autocorrelation function obtained from the SEM image and that from the experimental X-ray diffraction pattern. The radial streaking in the X-ray pattern, not present in the SEM-derived pattern, may be attributed to the missing disc of data in the center of the X-ray diffraction pattern.

Details of the iterative *HiO* algorithm used are given elsewhere (Fienup, 1982, 1987; Weierstall *et al.*, 2001). The scaling of the support mask is an important step in the data analysis. Several methods allow a scale to be applied to the diffraction pattern and its transform, including observation of the diffraction pattern from the silicon nitride window (whose dimensions are known) and calibration of the diffraction pattern using the known size of the balls. In fact, the most reliable method was found to be based on the autocorrelation function. Loops were drawn around each cluster in the SEM

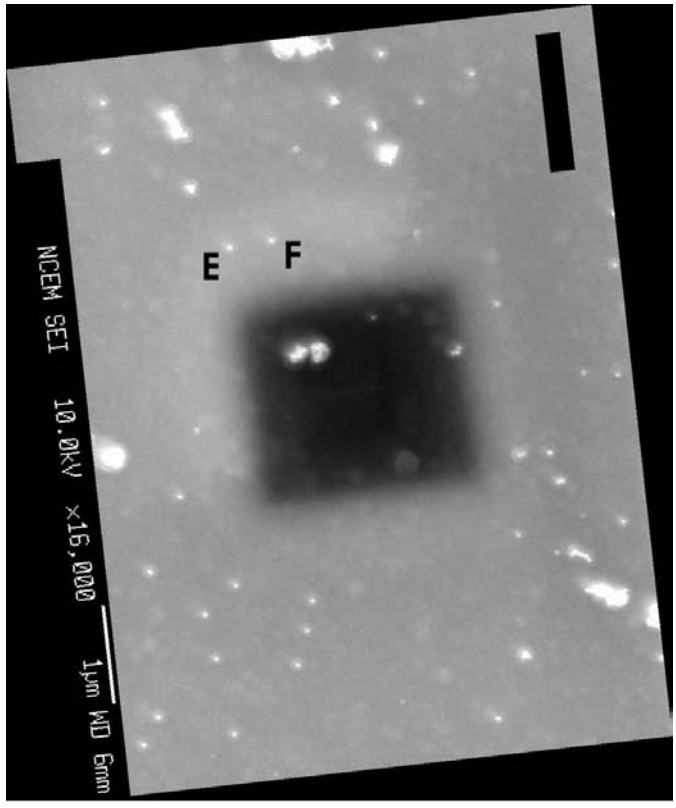

(*a*)

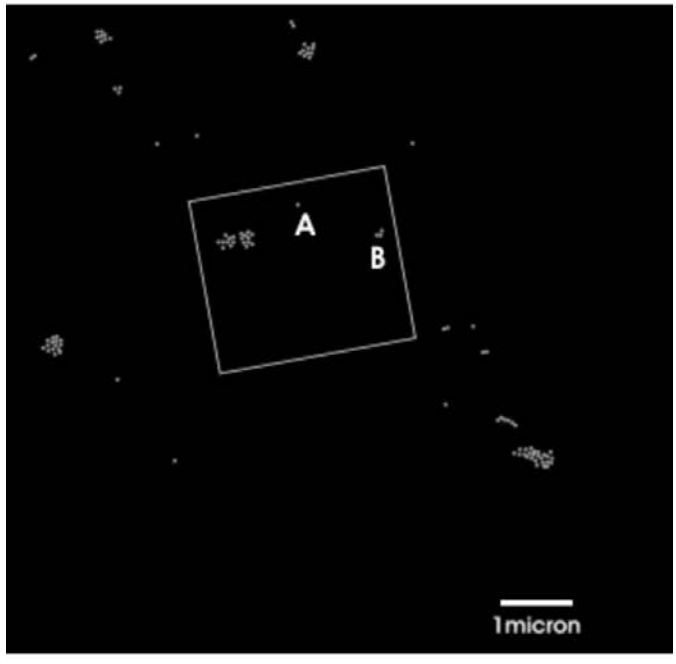

(*b*)

Figure 5
(*a*) SEM image (with correct orientation) of sample which produced the diffraction pattern in Fig. 2. The dark square in the center is the 100 nm-thick silicon nitride membrane. (*b*) Positions of balls extracted from SEM image in (*a*). The clusters seen in the autocorrelation function (Fig. 4*b*) are indicated as *A* and *B*.

image, and the autocorrelation function of this mask was then matched to the experimental autocorrelation function in orientation and magnification. This method is independent of the measurement of experimental parameters, and relies on the fact that our object consists of isolated clusters. More simply, the observation of two single-ball peaks in the (real-space) autocorrelation function can be used to scale the pattern.

Fig. 7 shows the result of applying the Fienup–Gerchberg–Saxton *HiO* algorithm alone to the experimental data of Fig. 2,

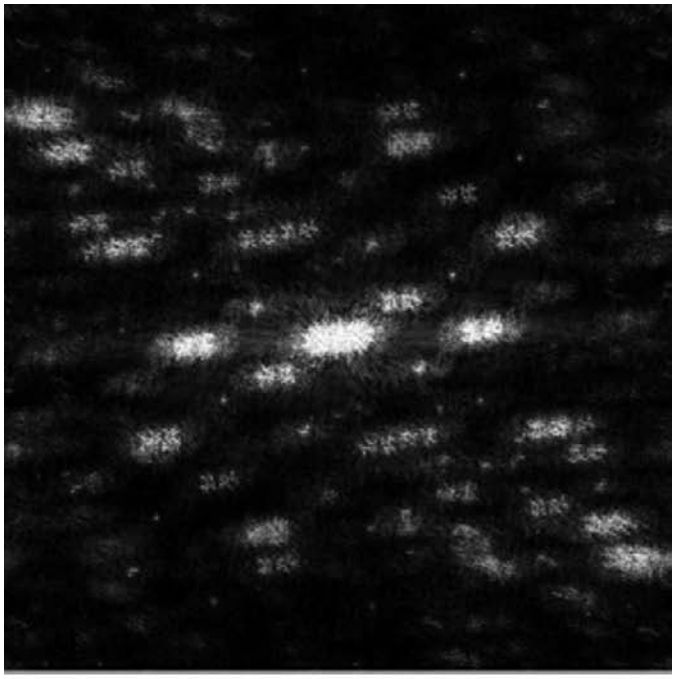

(*a*)

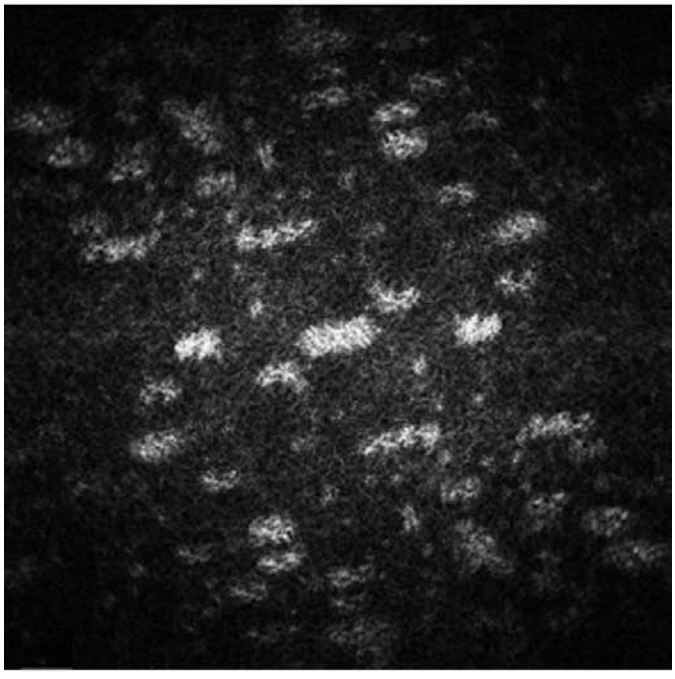

(*b*)

Figure 6
Comparison of (*a*) autocorrelation function obtained from SEM image (Fig. 4) and (*b*) that obtained from the experimental diffraction X-ray pattern shown in Fig. 2.

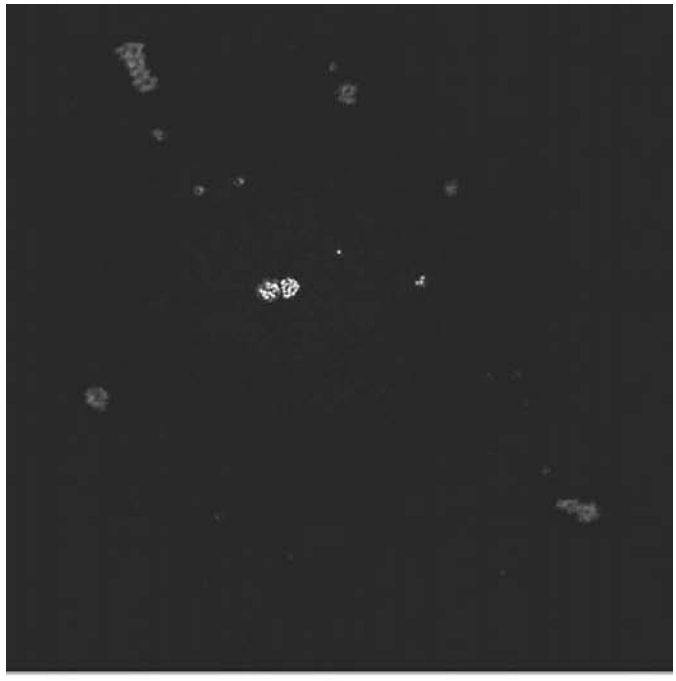

(*a*)

(*b*)

Figure 7
(*a*) Result of 150 iterations of the *HiO* algorithm applied to the experimental data in Fig. 2. Support used for the reconstruction is shown in (*b*) which is made by drawing around clusters in the SEM image. *HiO* extracts internal detail (see Fig. 8) of the unknown region shown in white. Note that balls imaged through the silicon frame around the edge are dimmer, owing to absorption [compare Fig. 5(*b*) with (*a*)].

while Figs. 8 and 9 show enlargements of the clusters and a comparison with the SEM images of the larger clusters. The same image was obtained when starting with a different set of random phases. The support mask used was obtained from loops drawn around each cluster seen in the SEM image. Regions of missing data in the diffraction pattern were first obtained by interpolation and then allowed to float during the iterations. A sign constraint was applied to both real and imaginary parts of the image at each iteration, which were made positive within loops. A feedback parameter value of 0.9 was used. Object areas outside the support loops drawn around clusters were set to zero rather than unity, and the floating zero-order Fourier coefficient used to find the average value of the image. More sophisticated image constraints were also tried, as discussed below. For balls lying on silicon, an additional phase shift can be expected from the silicon substrate – this phase shift reaches the value π for a thickness of 0.8 μm at 600 eV. Absorption will also be significant for balls imaged through the silicon – we note that the clusters reconstructed within the thin window area are much brighter than those outside.

Attempts to reconstruct the images using a support obtained by drawing around clusters in the autocorrelation function (using no information from the SEM image) were not successful.

4. Discussion

The reconstructed image obtained in Fig. 8 is seen to be a sharp image of the 50 nm diameter balls in roughly the correct positions they occupy in the corresponding SEM image. Owing to charging artifacts, balls were seen to move during the highest magnification SEM imaging of the large cluster, which may explain discrepancies. The resolution of the diffraction pattern in Fig. 2 from which the image is synthesized is about $R = 10$ nm, since the first zero of the ring pattern occurs at $1.394\lambda/d = 0.059$ rad $= \Theta_o$ ($d = 50$ nm, $\lambda = 2.11$ nm), and the pattern extends to $3\Theta_o = \lambda/R$. Image resolution is more difficult to define, since resolution was classically defined as a property of an instrument, not a sample. For coherent imaging of phase objects, as in this case, it depends on both, and therefore cannot strictly be defined in a sample-independent manner. Resolution also depends on noise and contrast, and is affected by the curvature of the Ewald sphere and the detector. The image was reconstructed in a manner consistent with the resolution in the diffraction pattern and the oversampling requirement, resulting in a pixel size of $W/1024 = 9$ nm or 5.5 pixels across the diameter of each 50 nm ball. To form this useful image, however, it was essential to know the approximate outline of each cluster. For experiments aimed at reconstructing images from the diffraction patterns of individual isolated molecules, this requirement need not be restrictive if the molecular size is known, and hence no secondary imaging would be required. We find that, for objects consisting of many clusters, the use of a support based on the autocorrelation function was not sufficient to provide a sharp image using this data.

The occurrence of single peaks in the autocorrelation pattern (Fig. 4) affords a simple interpretation of some features in this pattern. It indicates that clusters in the pattern can be found which are a simple convolution of a cluster with the image of a single ball, and so will show a direct image of every cluster, broadened by the image of one ball. (This is related to the method of Fourier transform holography.) Hence the preparation of a sample consisting of an isolated unknown object separated from an isolated gold ball by more than twice the size of the object would be invertible from the autocorrelation function alone (with resolution equal to the ball size). The coherence width must span the distance between ball and object. Macromolecules labeled with a single smaller gold ball might also be used.

The use of absorption filters and multiple exposures with different recording times has allowed us to record the entire diffraction pattern. The inner region of this pattern is dominated by the sinc-like diffraction pattern from the window

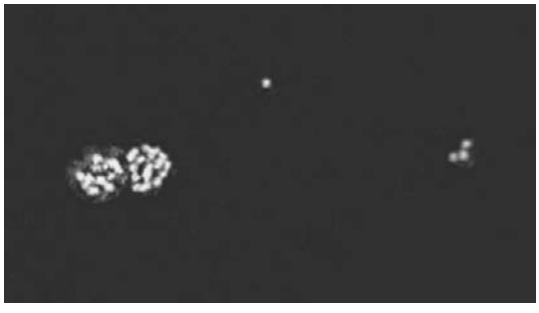

Figure 8
Enlargement of inner clusters shown in Fig. 7, showing internal detail.

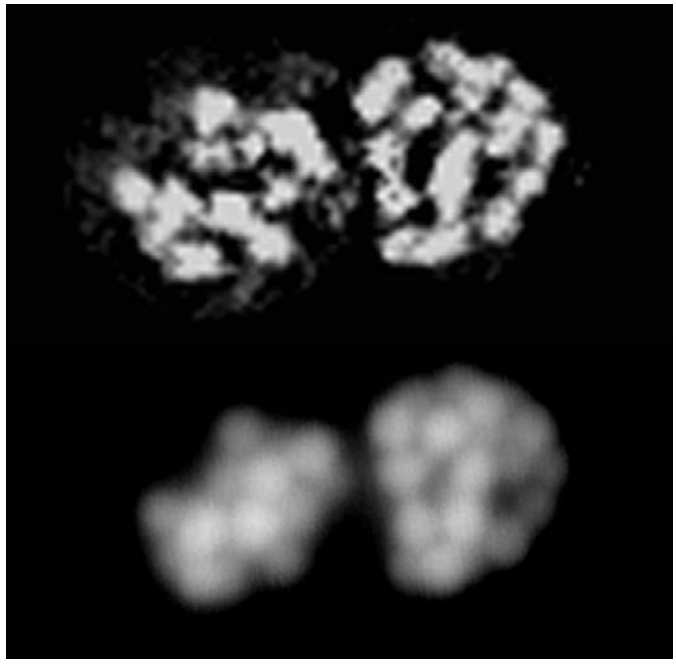

Figure 9
Enlargement of cluster *C* shown in Fig. 4(*b*), compared with SEM image (lower). The scale is set by the size of the balls in the SEM image, which have 50 nm diameter.

(and its wedge-shaped surroundings), and the algorithm was found to converge better if this region was excluded. Simulations clearly show that the loss of a small central region of the diffraction pattern does not prevent convergence of the algorithm.

More restrictive constraints were also tried but found to be less effective. These included constraining the image complex amplitudes at each pixel to a circle in the complex plane [unit modulus constraint, see equation (1)] or a spiral, if absorption is allowed. The use of a known histogram of image grey levels has also been suggested (Elser, 2003), and a 'binary object' constraint was tried. Here the balls are replaced by discs, and the object transmissivity allowed only two possible complex values.

Since balls outside the window clearly contributed to the pattern, we could not use the known window shape as a support. These outer balls introduce large phase shifts which violate our sign condition, and this may explain differences between the SEM image and the *HiO* image. Since we apply a sign constraint to both real and imaginary parts of the image (Miao *et al.*, 2001), our objects belong to the class of weak but complex objects. Convergence may have therefore been improved by our use of a disjoint support, which is found to be essential for true complex objects (large phase shifts). In order to understand the contribution of the wedge-shaped border to the center of the diffraction pattern, simulated diffraction patterns were obtained for the silicon window frame alone. This wedge introduces both phase and absorption contrast which will generate low-angle scattering. Using the known values of δ and β for silicon and the known wedge angle of 54°, a wedge transmission function was generated. The resulting simulated diffraction pattern is shown in Fig. 3(*b*), in good agreement with the experimental pattern in Fig. 3(*a*). We note in particular that the pattern does not have inversion symmetry, and the phase shifts used to simulate it exceed $\pi/2$ before absorption becomes severe. Attempts were made to incorporate this simulation into a complex support without success. Departures from Friedel symmetry in the data (required by the algorithm) could be caused by strains in the gold balls [see TEM images at atomic resolution (Smith, 1997)], by absorption in the silicon border, or by the occurrence of large phase shifts associated with the silicon border.

5. Conclusions

1. The preparation of an isolated object is the most experimentally demanding aspect of diffractive imaging. The use of μm-sized silicon nitride windows on single-crystal silicon frames, with samples dispersed on them from solution, addresses this problem. However, partial transparency of the surrounding region should be avoided, perhaps by using a large wedge angle or nano-fluidic techniques for sample deposition. The surface roughness of laser-drilled metal foil apertures is found to generate strong scattering, making them unsatisfactory. A crucial experimental problem for supported samples is ensuring that the scattering from the edges of the physical support window is less intense than that from the sample.

2. In this work, we found that a secondary low-resolution image was essential for defining the support function. The *HiO* algorithm then reproduced well the internal structure of the clusters at about 10 nm resolution, in reasonable agreement with SEM images of the same cluster. This secondary image may not be needed for the imaging of a single cluster of approximately known size, provided that the scattering is weak. The contribution to the diffraction pattern of balls outside the window may explain the failure of reconstruction using a support based on the autocorrelation function. By comparison with our previous work, these inversions of X-ray data are more successful than our inversions of experimental coherent electron diffraction patterns (Weierstall *et al.*, 2001), but less successful than our inversions of experimental visible light coherent diffraction patterns (Spence *et al.*, 2002). This trend would be explained by the relative experimental difficulty of ensuring that no objects outside the known support contribute to the diffraction pattern. For the visible light experiments, the object consisted of transparent shapes in an otherwise opaque mask.

3. Preparation of special objects containing an isolated gold ball near an unknown compact object are shown experimentally to allow simple image reconstruction without iteration based on the autocorrelation function by methods analogous to Fourier transform holography. This image may also provide a support function for the retrieval of higher-resolution images using the *HiO* algorithm.

4. The beam-stop problem, resulting in loss of low-order data in *HiO* imaging, may be avoided using calibrated absorption filters and multiple recording times.

5. If diffraction-pattern recording facilities are provided on zone-plate X-ray microscopes, resolution enhancement may be expected by combining image and diffraction data within the scheme of the *HiO* iterative algorithm, as demonstrated in the original Gerchberg–Saxton scheme.

This work was supported by the Director, Office of Energy Research, Office of Basic Energy Sciences, Materials Sciences Division of the US Department of Energy, under contract No. DE-AC03-76SF00098.

References

Barakat, R. & Newsam, G. (1984). *J. Math. Phys.* **25**, 3190–3193.
Bauschke, H., Combettes, P. L. & Luke, D. R. (2002). *J. Opt. Soc. Am.* **19**, 1334–1345
Cederquist, J. N, Fienup, J. R., Marron, J. C. & Paxman, R. G. (1988). *Optics Lett.* **13**, 619–621.
De Caro, L., Giacovazzo, C. & Siliqi, D. (2002). *Acta Cryst.* A**58**, 415–423.
Elser, V. (2003). *J. Opt. Soc. Am.* In the press.
Fienup, J. R. (1982). *Appl. Optics*, **21**, 2758–2769.
Fienup, R. (1987). *J. Opt. Soc. Am.* A**4**, 118–123.
Gerchberg, R. & Saxton, W. (1972). *Optik (Stuttgart)*, **35**, 237–249.
Howells, M., Charalambous, P., He, H., Marchesini, S. & Spence, J. (2003). In *Design and Microfabrication of Novel X-ray Optics*, edited by D. Mancini. Beligham: SPIE. In the press.

Howells, M. R., Calef, B., Jacobsen, C. J., Spence, J. H., Yun, W. (1999). In *A Modern Approach to X-ray Holography*, edited by A. Warwick. Berkeley, CA: American Institute of Physics.
Kamura, Y. & Komatsu, S. (1998). *Jpn. J. Appl. Phys.* **37**, 6018–6019.
Liao, C., Fiddy, M. & Byrne, C. (1997). *J. Opt. Soc. Am.* A**14**, 3155–3161.
Miao, J., Charalambous, C., Kirz, J. & Sayre, D. (1999). *Nature (London)*, **400**, 342–344.
Miao, J., Hodgson, K. & Sayre, D. (2001). *Proc. Natl Acad. Sci. USA*, **98**, 6641–6645.
Miao, J., Ishikawa, T., Johnson, E. H., Lai, B. & Hodgson, K. (2002). *Phys. Rev. Lett.* **89**, 088303, 1–4.
Millane, R. (1990). *J. Opt. Soc. Am.* **7**, 394–411.
Millane, R. (1993). *J. Opt. Soc. Am.* A**10**, 1037–1045.
Paganin, D. & Nugent, K. (1998). *Phys Rev Lett.* **80**, 2586–2589.
Robinson, I. K., Vartanyants, I. A., Williams, G. J., Pfeifer, M. A. & Pitney, J. A. (2001). *Phys. Rev. Lett.* **87**, 195505, 1–4.
Sayre, D. (1952). *Acta Cryst.* **5**, 843.
Sayre, D. (1980). *Image Processing and Coherence in Physics. Springer Lecture Notes in Physics*, Vol. 112, edited by M. Schlenker, pp. 229–235. Berlin: Springer.
Sayre, D., Chapman, H. & Miao, J. (1998). *Acta Cryst.* A**54**, 232–239.
Smith, D. J. (1997). *Rep. Prog. Phys.* **60**, 1513–1580.
Spence, J., Weierstall, U. & Howells, M. (2002). *Philos. Trans. R. Soc. London*, **360**, 1–21.
Spence, J. C. H. (2003). *High Resolution Electron Microscopy*. New York: Oxford University Press.
Spence, J. C. H., Howells, M., Marks, L. D. & Miao, J. (2001). *Ultramicroscopy*, **90**, 1–6.
Stark, H. (1987). *Image Recovery: Theory and Applications.* New York: Academic Press.
Weierstall, U., Chen, Q., Spence, J., Howells, M., Isaacson, M. & Panepucci, R. (2001). *Ultramicroscopy*, **90**, 171–195.